Supplementary Information for

Crustal melting and continent uplift by mafic underplating at convergent boundaries

Zhipeng Zhou[1], Hans Thybo[1,2,3*], Irina M. Artemieva[1,3,4*], Timothy Kusky[3,5] & Chi-Chia Tang[6]

[1]SinoProbe Lab, Chinese Academy of Geological Sciences, 100037 Beijing, China

[2]Eurasia Institute of Earth Science, Istanbul Technical University, 34469 Istanbul, Turkey

[3]GPMR State Key Lab, School of Earth Sciences, China University of Geosciences, 430074 Wuhan, China

[4]Section of Marine Dynamics, GEOMAR Helmholtz Center for Ocean Research, 24148 Kiel, Germany

[5]Center for Global Tectonics and Badong National Observation and Research Station of Geohazards, China University of Geosciences, 430074 Wuhan, China

[6]School of Geophysics and Geomatics, China University of Geosciences, 430074 Wuhan, China

*Corresponding authors: H. Thybo, h.thybo@gmail.com; I. M. Artemieva, iartemieva@gmail.com
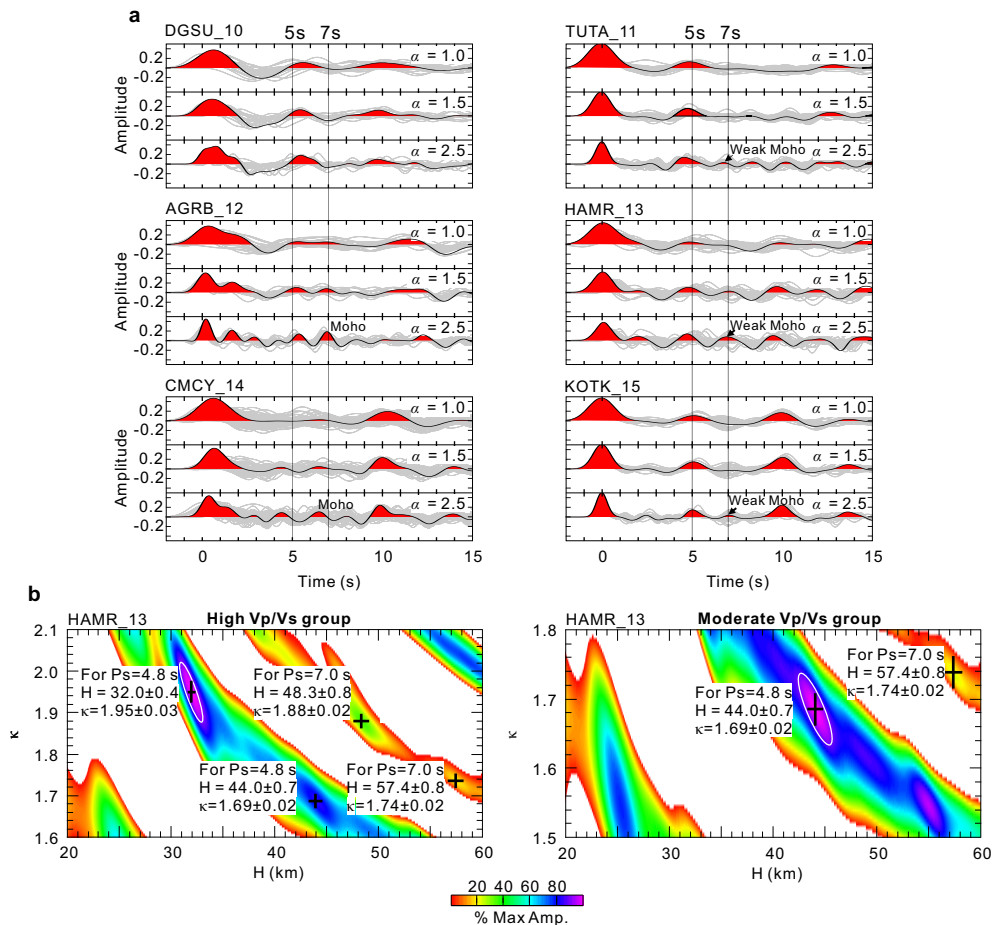
The supplementary information includes:
Supplementary Figures 1-12
Supplementary Tables 1-3
Supplementary References

Supplementary Figures

Supplementary Fig. 1. RFs for six stations in EAP and an example of H-κ stacking. a P-wave RFs filtered with Gaussian filters for α=1.0, 1.5, and 2.5, corresponding to cutoff frequencies of 0.48, 0.72, and 1.24 Hz, respectively. The individual RFs are represented by grey wiggles, while the stacked RFs are represented by black wiggles with red positive converters. **b** H-κ stack for station HAMR_13 displayed for two different κ intervals. H is the crustal thickness which is the sum of Moho depth and topography, and κ=Vp/Vs. Left: For a Ps converter at 4.8 s, the maximum stacking amplitude occurs at κ=1.95 and H=32.0 km. Similarly, for a Ps converter at 7.0 s, the maximum stacking amplitude occurs at κ=1.88 and H= 48.3 km. Right: For the search range κ<1.80, the maximum stacking amplitude for a Ps converter at 4.8 s occurs at κ=1.69 and H=44.0 km. Our preferred crustal thickness is 48.3 km after interpolation based on gravity data (Supplementary Fig. 11).
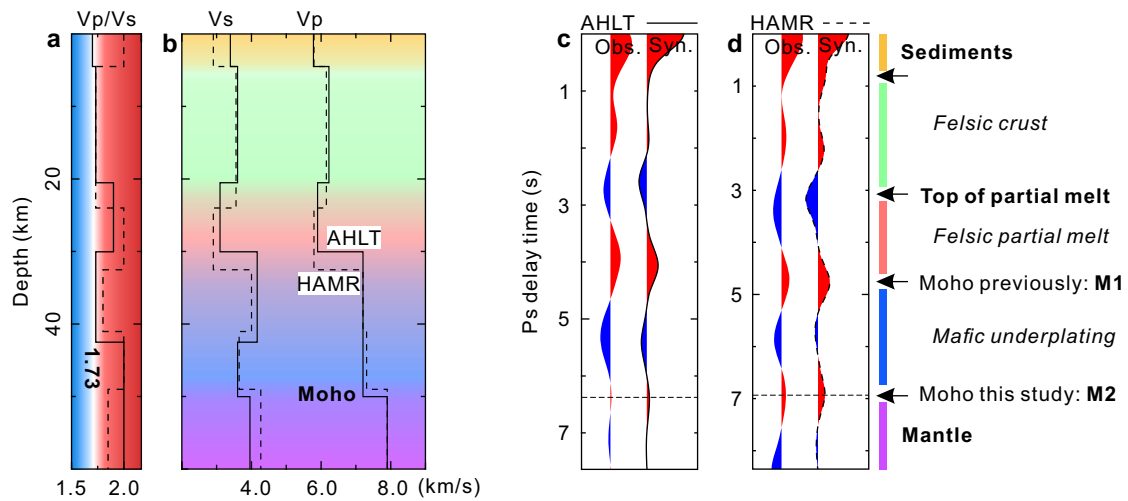
Supplementary Fig. 2. Comparison between observed and synthetic RFs. Station locations are shown in Fig. 1. **a, b** Velocity models for calculation of synthetic RFs; solid line - station AHLT, dashed line - station HAMR. Red area in Vp/Vs with high ratios is typical of middle crust with partially molten bodies around depths of 20-30 km. **c**, **d** Comparison between the synthetic (right) and observed RFs (left) for the two stations.
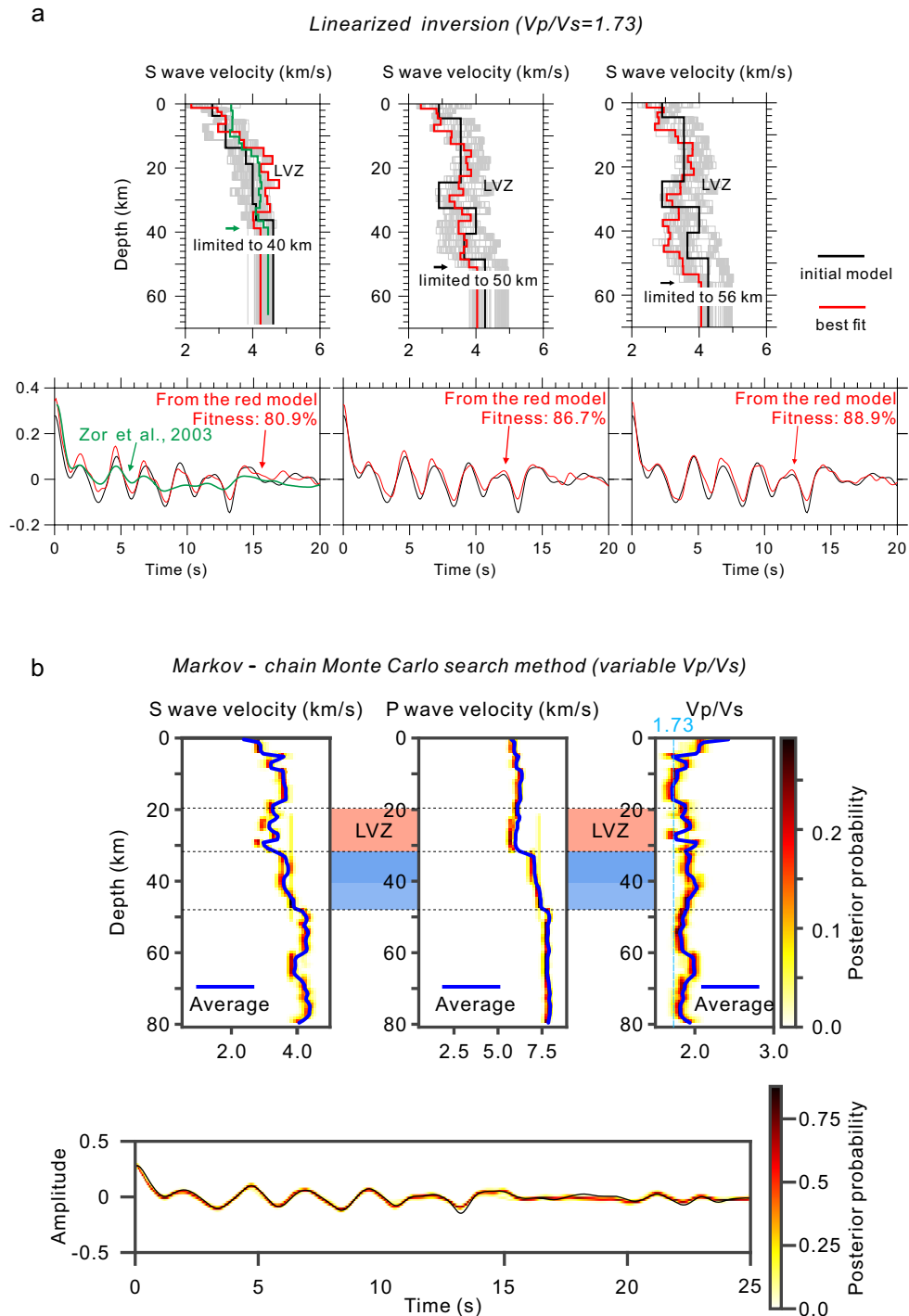
Supplementary Fig. 3. Velocity inversion of RF for station HAMR based on linear and non-linear methods. a Linear inversion[1] with a Gaussian filter of 2.5. Upper panels: Left panel shows the inversion result for the same parameters as used in an earlier study[2]. Middle and right panels show results for deeper ranges of the parameter space set to 50 and 56 km, respectively. Lower panels show the fit between observed RF (black line) and synthetic RF for the model resulting from the inversion (red line). **b** Inversion of RF by the transdimensional Markov – chain Monte Carlo (MCMC) method[3] for an initial model as in Supplementary Fig. 2b. Upper panels show resulting vertical Vs,

Vp, and Vp/Vs profiles, illustrated by probabilities with the average models shown by blue line; depths to the two main crustal layers are illustrated. Lower panel shows the correlation between observed RF (black line) and the RFs considered by the inversion algorithm, illustrated by probability.
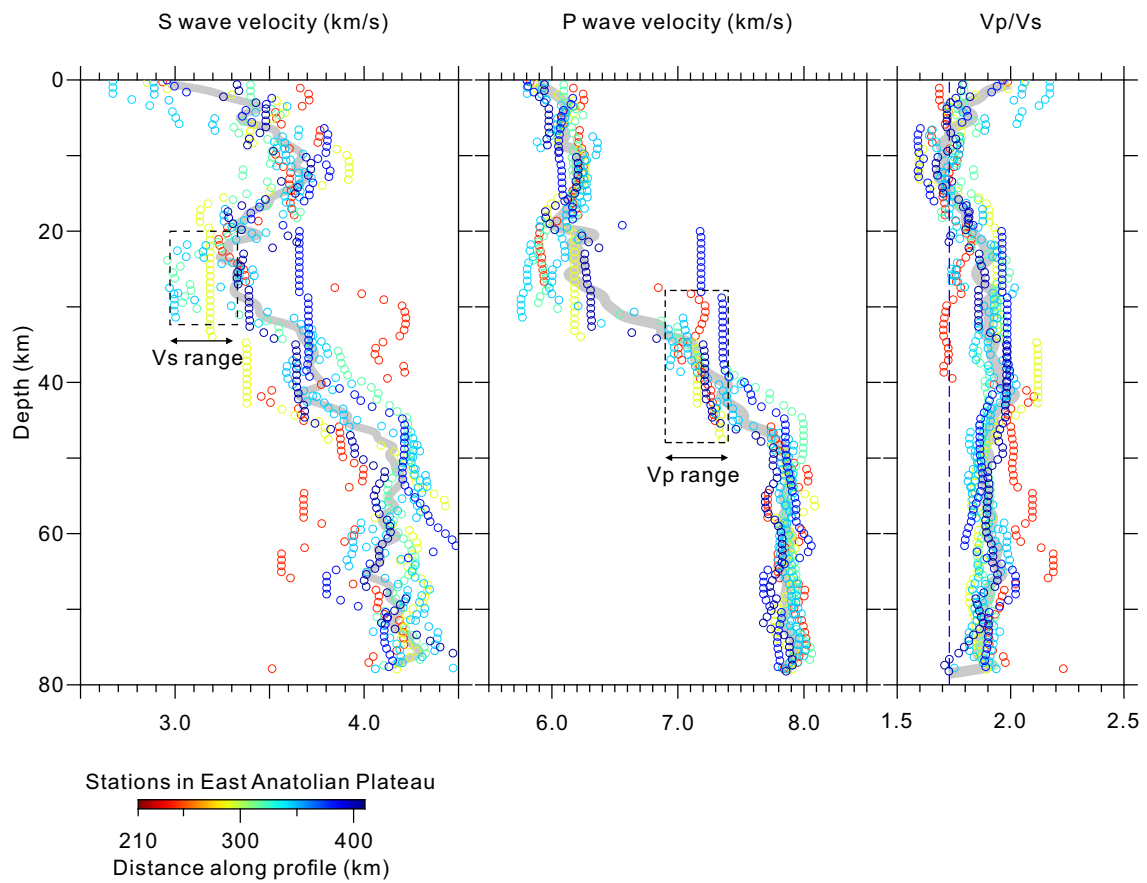
Supplementary Fig. 4. Vertical Vs, Vp, and Vp/Vs profiles obtained from MCMC inversion of the RFs at the seismic stations in EAP. Vertical profiles are shown for individual stations (colour-coded). Dashed boxes **-** typical Vs variation in the low-velocity layer at 20-30 km depth, and Vp variation at 30-50 km depth in the high velocity lower crust.
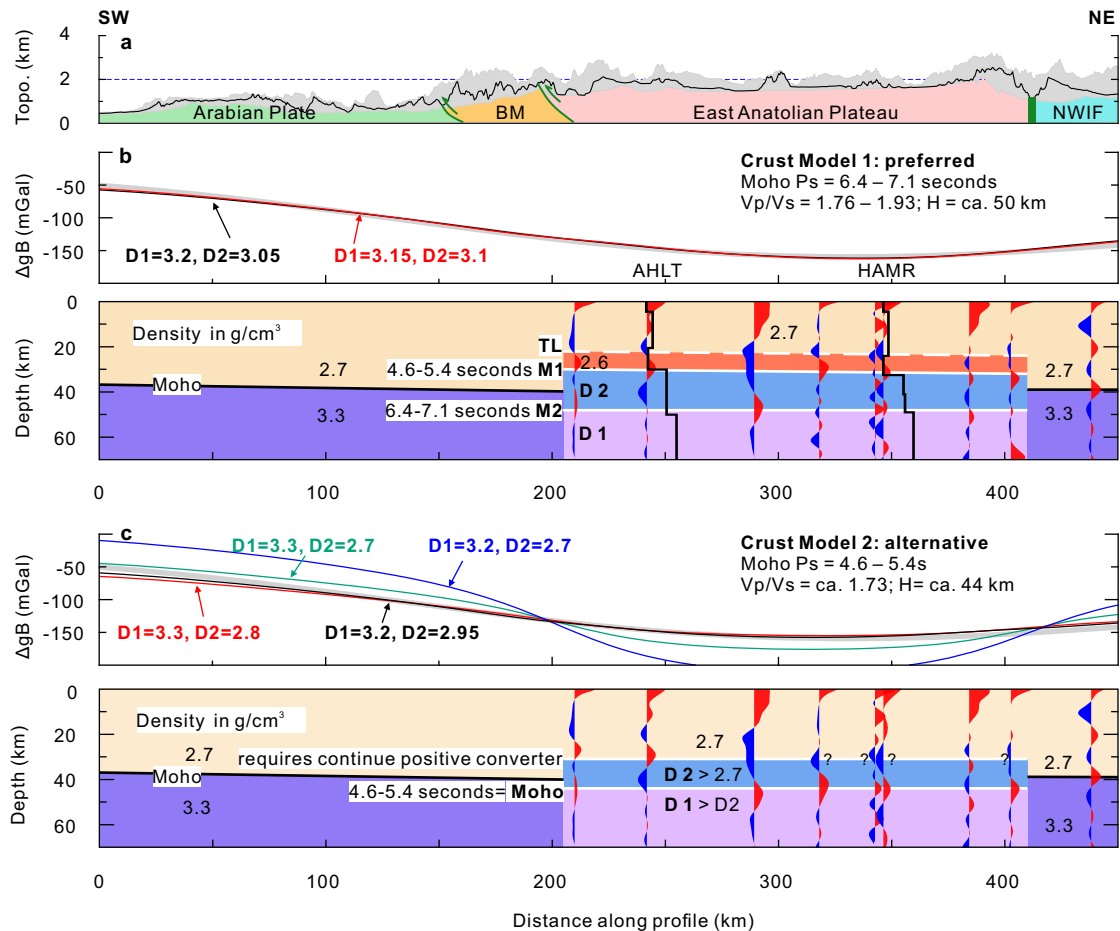
Supplementary Fig. 5. Gravity test across the EAP. **a** Topography within a ±40 km-wide corridor along the profile (in grey) with actual topography along the profile in black. Abbreviations: BM – Bitlis Massif, NWIF – NW Iranian Fragment. **b**, **c** Long-wavelength filtered Bouguer gravity anomaly (thick grey line) with calculated gravity response for two models corresponding to different density values (in g/cm^3) of the lower crust (D2) and upper mantle (D1). **b** Preferred crustal model with Moho at M2 (bottom panel); it is consistent with the RF phases and the velocity model derived from synthetic RF test (thick vertical black lines). The exact density of the lower crust depends on the mantle density. D2=3.05 g/cm^3 for the underplated lower crust if D1=3.20 g/cm^3 for the hot mantle[4-7]. D2=3.10 g/cm^3 for the underplated lower crust if D1=3.15 g/cm^3 for an extremely hot mantle, as indicated by the extremely weak Ps converter. **c** Alternative, unrealistic model assuming that the Moho corresponds to earlier interpreted, strong Ps phase at about 5 seconds at M1 (Vp/Vs ≈ 1.73; H ≈ 44 km). The required lower crustal density of 2.70 g/cm^3 makes it impossible to fit the gravity anomaly (blue and green lines in the upper panel). Instead, a lower crust with a density of 2.95 g/cm^3 is required to match the hot mantle density of

3.20 g/cm^3, in which case the amplitude of the calculated Ps phase for Moho will be weak. Further, continuous positive Ps converters should be observed at the top of the high-density lower crust, but the RFs show a continuous negative Ps converter (marked by question marks). Therefore, this "alternative" model is unrealistic.
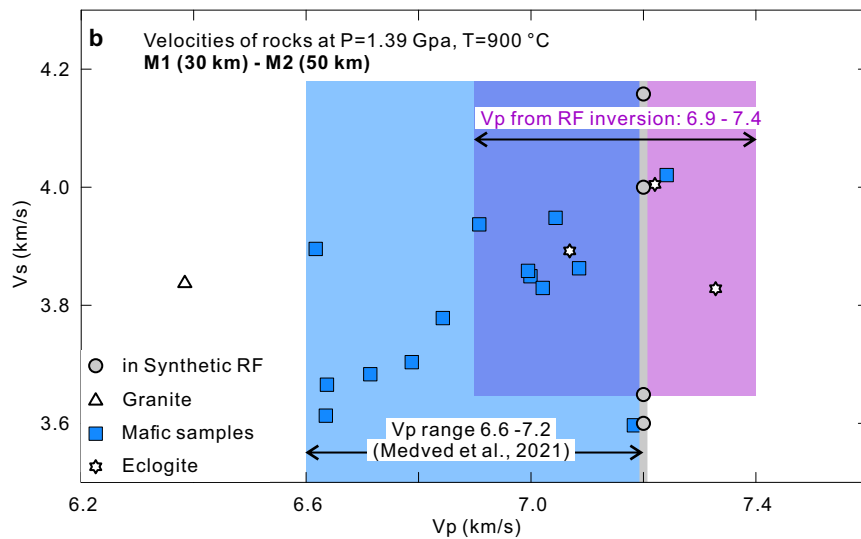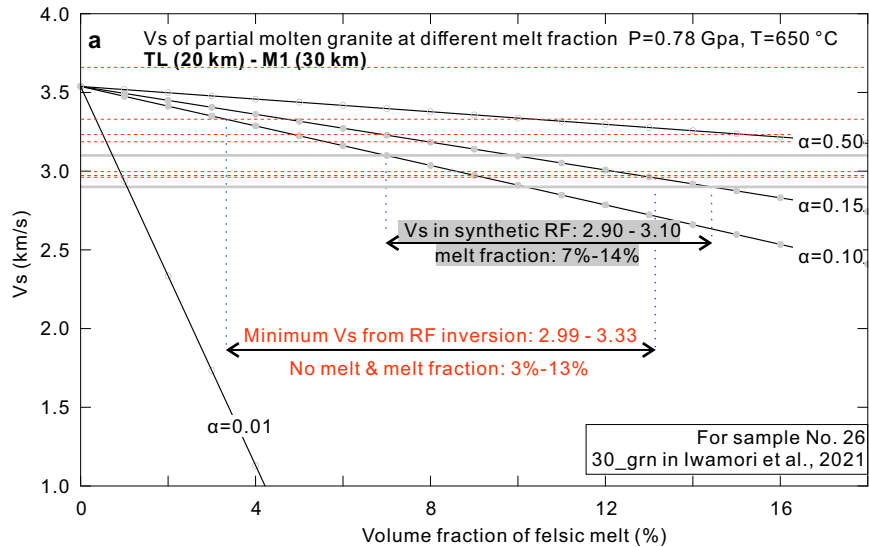
Supplementary Fig. 6. Petrological interpretation of seismic wave velocities. a S-wave velocity (Vs) versus fraction of granitic melt[8] at temperature and pressure conditions corresponding to 30 km depth in EAP. For a dihedral angle of 20–40° and aspect ratio of melt inclusions α=0.10–0.15[9], Vs=3.0±0.1 km/s corresponds to 7–14% partial melt. Our observed Vs of 2.96-3.33 km/s corresponds to 3-13% melt, and Vs=3.5 km/s corresponds to a melt-free environment. **b** Vs versus Vp based on our seismic-gravity results (circles) together with literature data[8] for granites, mafic rocks and eclogites (see legend). Blue area cover the intervals observed in seismic tomographic models[10]. Most of the mafic rocks, including amphibolite and gabbro, have Vp in the interval of 6.6–7.2 km/s, which correspond to the values in a tomographic P-wave velocity model[10] for the lower crust as well as our synthetic RF model (7.2 km/s).
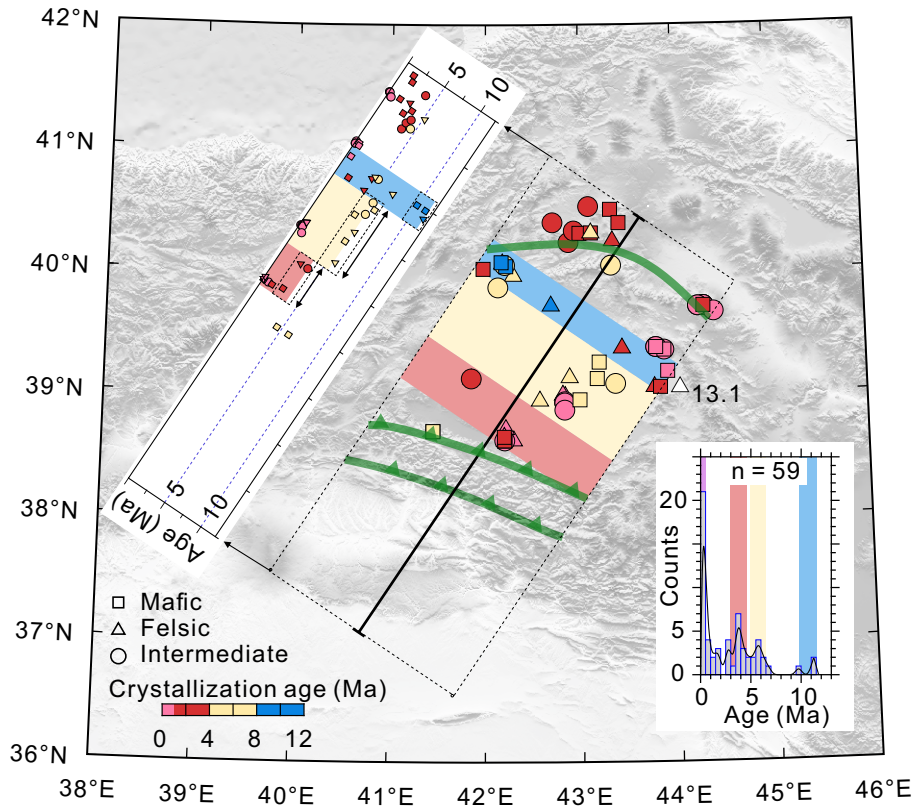
Supplementary Fig. 7. Distribution of magmatic ages ≤12 Ma in a ±100 km-wide corridor (dotted lines) along the profile. Magmatic activity began in the north at about 12 Ma and progressed southward with time.
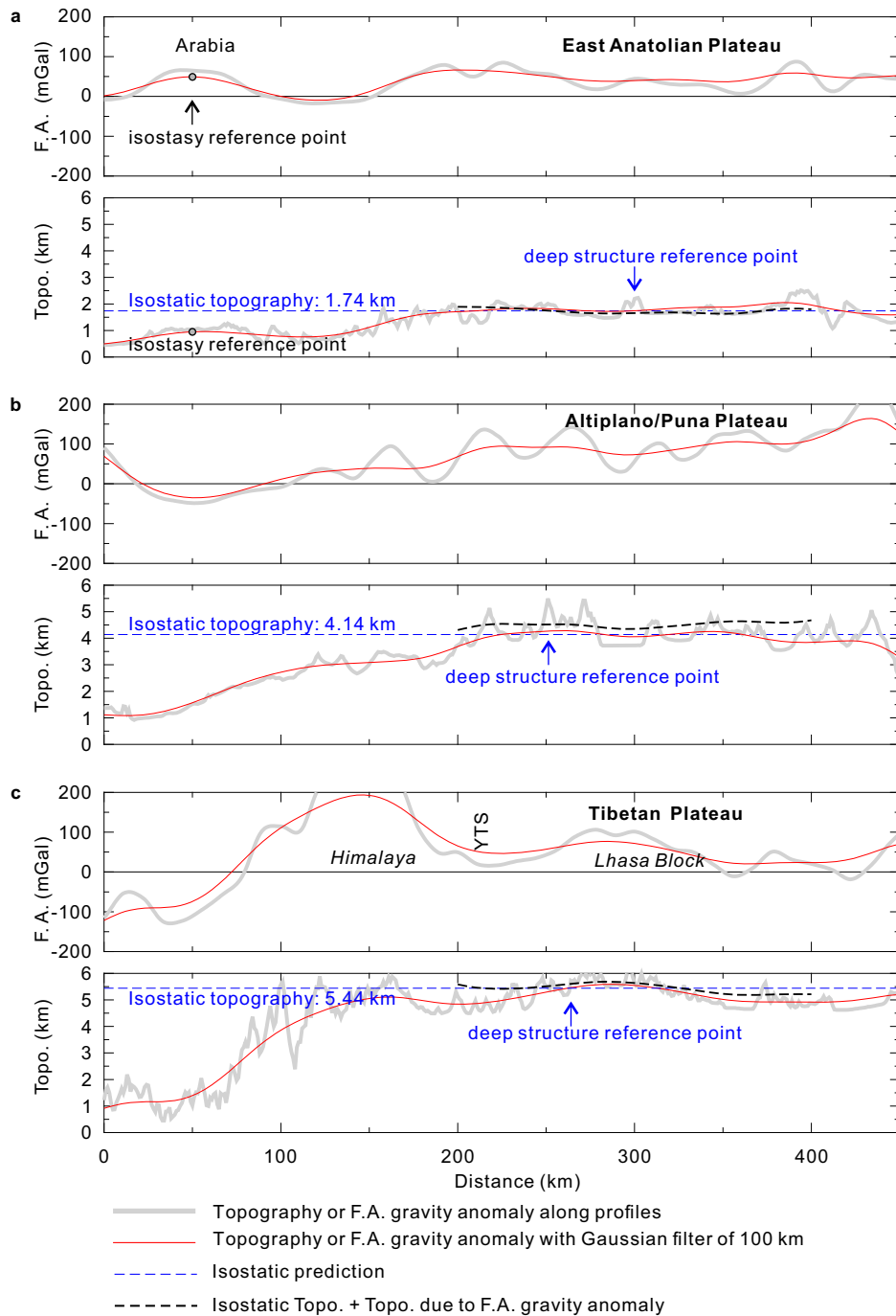
Supplementary Fig. 8. Free air gravity anomaly and topography in (a) EAP, (b) Andes and (c) Tibet (cf. Fig. 5). For each location upper panel shows observed (grey line) and smoothed (red line) free air (F.A.) gravity anomaly. Lower panel shows observed (grey line) and smoothed (red line) topography together with topography calculated by assuming isostasy for the models in Fig. 5 (stippled blue line), and additionally taking the smoothed free air gravity anomaly into account (stippled black line). All smoothing is done by wavelength filtering with a cut-off at 48 km. Note that the isostatic topography is calculated at reference points with horisontal crustal layers.
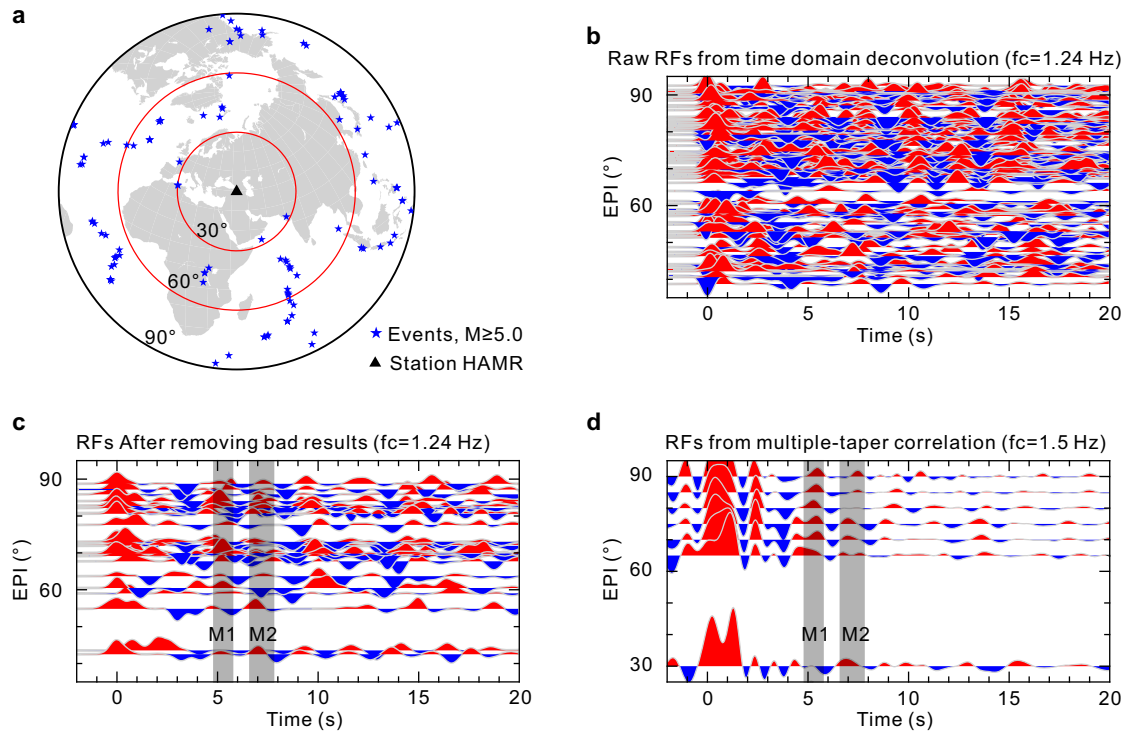
Supplementary Fig. 9. RFs calculated with different deconvolution methods. **a** Event distribution for station HAMR. **b** Initial radial RF results based on time-domain interactive deconvolution[11]. **c** Selected RFs, after quality check, with the P wave arrival time aligned at zero time. **d** Radial RFs by multiple-taper correlation (MTC)[12] calculated in the frequency domain and stacked in 5-degree bins. The two methods lead to comparable results.
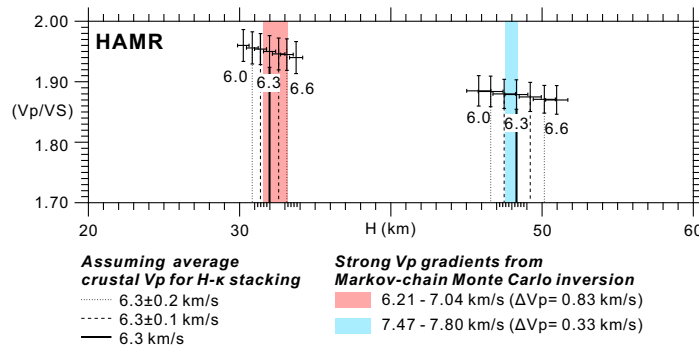
Supplementary Fig. 10. Sensitivity analysis of H-κ stacking at station HAMR versus average crustal Vp. Black error bars show best fit solution with uncertainty based on H-k stacking with Vp between 6.0 and 6.6 km/s, colored bars – uncertainty based on the result from transdimensional MCMC inversion. Average uncertainty of ±0.2 km/s in crustal Vp corresponds to a deph uncertainty of ±1.2 km at ~30 km depth (bottom of layer with partially molten pockets) and to ±1.7 km ~50 km depth (Moho interface). H values calculated for average crustal Vp=6.3 km/s fit the two velocity jumps in the RF inversion.
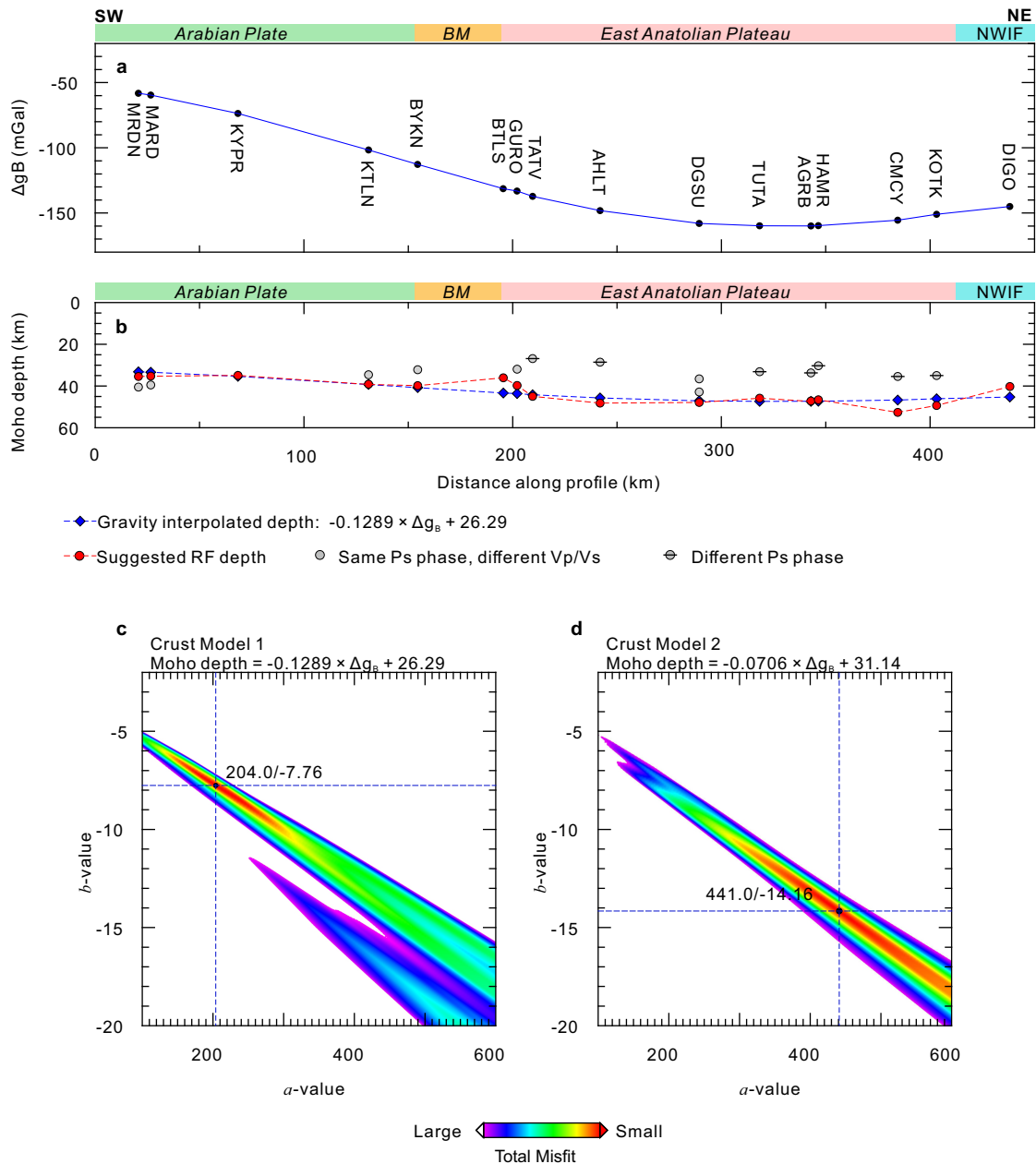
Supplementary Fig. 11. Best fit empirical parameters linking Bouguer gravity anomaly with RF Moho depth in EAP. a Long-wavelength Bouguer gravity anomaly along the profile in Fig. 1 with stations marked by black dots. **b** All possible Moho depths from H-k stacking for either different Vp/Vs (red and grey circles) or different Ps phases (crossed grey circles). Blue symbols show the gravity interpolated depths. Stippled line through red points show preferred Moho depth based on the gravity interpolation method[13]. This method assumes a local linear relationship $D=(\Delta g_B - a)/b$ between the Bouguer gravity anomaly (Δg_B) and the depth to the Moho (D), and parameters a and b are determined empirically from the data. **c, d** Empirically a and b are determined by different RF candidates in Supplementary Table 1: **c** High Vp/Vs group, **d** Moderate Vp/Vs group.
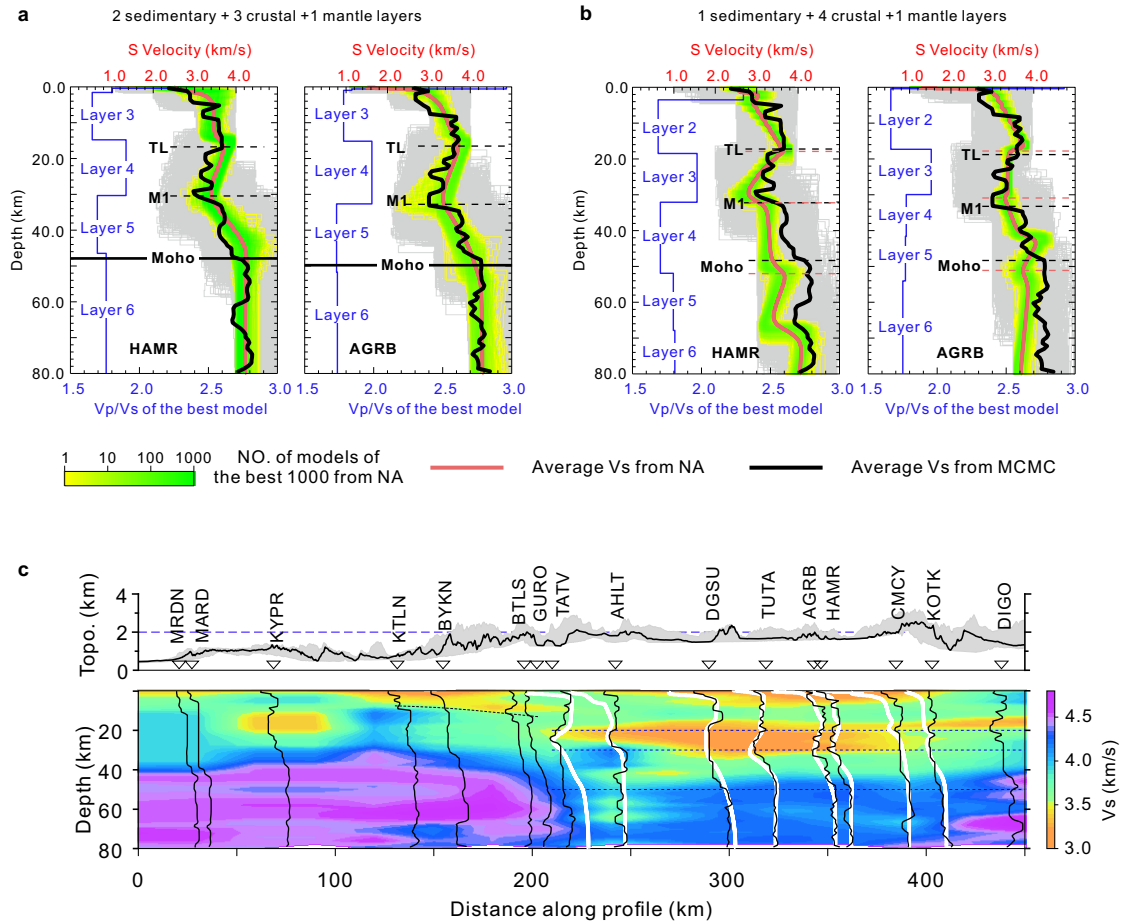
Supplementary Fig. 12. Constraints on the vertical extent of LVZs by two non-linear inversion algorithm. a, **b** Average Vs models inverted by the Neighbourhood Algorithm (NA)[14,15] and transdimensional MCMC algorithm. For NA: the Vp/Vs for the best-fit velocity structure is shown by blue lines, the yellow-green gradient density plots illustrate the proportion of better-fitting models in that region. **a** Using the default velocity search parameters, the inversion result by NA and MCMC algorithm show strong agreement, except that the NA cannot identify the lower LVZ due to its limitation to six layers. **b** Merging the uppermost 2 layers into a single layer for the NA allows detection of the lower LVZ in the mantle, and the NA inversion results show same velocity jump at results from MCMC although the absolute values are shifted. **c** Plot of the MCMC result (black lines) as in Fig. 3c with the result from the NA in white (using the same searching parameters as in **a**). The depth and vertical extent of the low-velocity layer beneath each station are similar for the two non-linear inversion methods.

Supplementary Table 1. Details of the RF interpretation. Symbols "#" and "*" after the acquisition period refer to sources of data (IRIS and Kandilli Observatory, respectively), Δg_B = Bouguer gravity anomaly. The bold H-κ pairs are the final values selected in this paper.

Duration	St._No.	Lon. (°)	Lat. (°)	Ele. (m)	Δg_B (mGal)	RFs: Ps delay time (s) | Amplitude					One Ps with multiple H-κ pairs H-κ (Ps)			High Vp/Vs group H-κ (Ps)		Moderate Vp/Vs group H-κ (Ps)	
1999-2001#	MRDN_1	40.70	37.29	674	-58.2	(4.7 | 0.06)	(5.9 | 0.01)	(7.7 | 0.02)			**36.1-1.78 (4.7s)**	41.2-1.68 (4.7s)					
2008-2009*	MARD_2	40.78	37.31	1290	-59.6	(3.1 | 0.01)	(5.1 | 0.09)	(6.7 | 0.00)			**36.5-1.84 (5.1s)**	40.8-1.75 (5.1s)					
1999-2001#	KYPR_3	41.17	37.56	1179	-73.6	(3.1 | 0.02)	(4.4 | 0.09)	(6.5 | 0.03)	(9.8 | 0.04)		**36.1-1.79 (4.4s)**						
1999-2001#	KTLN_4	41.71	37.95	791	-101.6	(4.5 | 0.07)					**39.9-1.71 (4.5s)**	35.4-1.80 (4.5s)					
1999-2001#	BYKN_5	41.78	38.17	816	-112.7	(4.6 | 0.11)	(9.7 | 0.08)				**40.6-1.69 (4.6s)**	33.0-1.85 (4.6s)					
1999-2001#	BTLS_6	42.12	38.43	1722	-131.3	(5.4 | 0.11)					**37.8-1.89 (5.4s)**						
2012-2012#	GURO_7	42.03	38.55	1388	-133.1	(5.9 | 0.10)					**41.1-1.88 (5.9s)**	33.3-2.08 (5.9s)					
2008-2009*	TATV_8	42.27	38.51	1831	-137.3	(3.6 | 0.17)	(6.0 | 0.07)	(9.1 | 0.01)						28.7-1.75 (3.6s)	**46.8-1.75 (6.0s)**		
1999-2001#	AHLT_9	42.48	38.75	1738	-148.2	(4.0 | 0.13)	(6.4 | 0.01)	(8.0 | 0.02)	(9.6 | 0.05)					30.3-1.77 (4.0s)	**49.9-1.76 (6.4s)**		
1999-2001#	DGSU_10	42.73	39.13	1646	-158.0	(5.5 | 0.09)	(8.2 | 0.01)	(9.8 | 0.06)			**49.5-1.68 (5.5s)**	44.5-1.75 (5.5s)	38.2-1.88 (5.5s)				
2008-2009*	TUTA_11	42.81	39.40	2154	-159.8	(4.6 | 0.12)	(6.8 | 0.03)	(8.4 | 0.04)						35.3-1.80 (4.6s)	**48.0-1.88 (6.8s)**	40.2-1.70 (4.6s)	56.0-1.75 (6.8s)
2011-2011*	AGRB_12	42.99	39.58	1820	-159.9	(3.0 | 0.05)	(4.3 | 0.00)	(5.4 | 0.12)	(6.9 | 0.16)	(8.6 | 0.01)				35.5-1.89 (5.4s)	**49.0-1.84 (6.9s)**	44.4-1.71 (5.4s)	56.7-1.72 (6.9s)
1999-2001#	HAMR_13	42.99	39.61	1714	-159.6	(4.8 | 0.10)	(7.0 | 0.06)	(9.6 | 0.07)						32.0-1.95 (4.8s)	**48.3-1.88 (7.0s)**	44.0-1.69 (4.8s)	57.4-1.74 (7.0s)
1999-2001#	CMCY_14	43.20	39.92	1995	-155.5	(3.1 | 0.00)	(4.5 | 0.04)	(6.5 | 0.05)	(8.1 | 0.01)	(9.9 | 0.11)						37.4-1.72 (4.5s)	**54.6-1.73 (6.5s)**
1999-2001#	KOTK_15	43.01	40.22	1396	-150.9	(5.1 | 0.07)	(7.1 | 0.02)							36.4-1.87 (5.1s)	**50.7-1.85 (7.1s)**	44.4-1.71 (5.1s)	57.4-1.75 (7.1s)
2009-2009*	DIGO_16	43.37	40.41	2278	-145.0	(3.1 | 0.14)	(5.2 | 0.22)	(7.4 | 0.05)	(9.4 | 0.11)		**42.5-1.75 (5.2s)**						

Supplementary Table 2. Parameters for linear inversion of station HAMR.

maximum cubic perturbation	0.75
stop perturbing at this velocity (km/s)	8.5
maximum random perturbation (in % of cubic perturbation)	20
number of iterations per inversion	4
smoothness trade-off parameter	0.1
number of inversions (x 4 perturbation scheme)	24 (x 4)
singular value truncation fraction	0.01
high-pass filter the waveforms (y or n)	n
horizontal slowness (ray parameter)	0.06
waveform delay	0
gaussian width factor	2.5

Supplementary Table 3. Parameters for transdimensional Markov – chain Monte Carlo inversion.

N_BURN: iteration number during a burn-in period	300000
N_ITER: iteration number after the burn-in period	800000
interval of iterations to save sampled model	200
start and end of time window to be analysed	0-25
Parameter choice for the prior probabilities	
Min. and Max. of interfaces	1-41
Min. and Max. of interface depth (km)	0-80
Min. thickness of layer to be allowed	0.05
standard deviation for dVs prior (km/s)	0.1
standard deviation for dVp prior (km/s)	0.1
Parameter choice for proposals	
fixed noise level	0.01
standard deviation for depth (km)	0.02
standard deviation for dVs (km/s)	0.01
standard deviation for dVp (km/s)	0.01
Additional criteria	
VP range	0.5-8.9
VS range	0.5-5.0
VP/Vs range	1.5-3.0
Initial velocity model	
Stations within EAP	Supplementary Fig. 2
Stations outside EAP	ak135 Earth Model

Supplementary References

1. Ammon, C. J., Randall, G. E. & Zandt, G. On the nonuniqueness of receiver function inversions. *J. Geophys. Res.* **95**, 15303-15318 (1990).
2. Zor, E. et al. The crustal structure of the East Anatolian plateau (Turkey) from receiver functions. *Geophys. Res. Lett.* **30**, 8044 (2003).
3. Akuhara, T., Tsuji, T. & Tonegawa, T. Overpressured underthrust sediment in the Nankai Trough Forearc inferred from transdimensional inversion of high‐frequency teleseismic waveforms. *Geophys. Res. Lett.* **47**, e2020GL088280 (2020).
4. Gök, R., Pasyanos, M. E. & Zor, E. Lithospheric structure of the continent-continent collision zone: eastern Turkey. *Geophys. J. Int.* **169**, 1079-1088 (2007).
5. Zhu, H. High Vp/Vs ratio in the crust and uppermost mantle beneath volcanoes in the central and eastern Anatolia. *Geophys. J. Int.* **214**, 2151-2163 (2018).
6. Al-Lazki, A. I. et al. Tomographic Pn velocity and anisotropy structure beneath the Anatolian plateau (eastern Turkey) and the surrounding regions. *Geophys. Res. Lett.* **30**, 8043 (2003).
7. Mutlu, A. K. & Karabulut, H. Anisotropic Pn tomography of Turkey and adjacent regions. *Geophys. J. Int.* **187**, 1743-1758 (2011).
8. Iwamori, H. et al. Simultaneous Analysis of Seismic Velocity and Electrical Conductivity in the Crust and the Uppermost Mantle: A Forward Model and Inversion Test Based on Grid Search. *J. Geophys. Res. Solid Earth* **126**, e2021JB022307 (2021).
9. Takei, Y. Effect of pore geometry on VP/VS: From equilibrium geometry to crack. *J. Geophys. Res. Solid Earth* **107**, 2043 (2002).
10. Medved, I., Polat, G. & Koulakov, I. Crustal Structure of the Eastern Anatolia Region (Turkey) Based on Seismic Tomography. *Geosciences* **11**, 91 (2021).
11. Ligorria, J. P. & Ammon, C. J. Iterative deconvolution and receiver-function estimation. *B. Seismol. Soc. Am.* **89**, 1395-1400 (1999).
12. Park, J. & Levin, V. Receiver Functions from Multiple-taper spectral correlation estimates. *B. Seismol. Soc. Am.* **90**, 1507-1520 (2000).
13. Zhou, Z., Thybo, H., Tang, C., Artemieva, I. & Kusky, T. Test of P-wave receiver functions for a seismic velocity and gravity model across the Baikal Rift Zone. *Geophys. J. Int.* **232**, 176-189 (2023).
14. Sambridge, M. Geophysical inversion with a neighborhood algorithm—I. Searching a parameter space. *Geophys. J. Int.* **138**, 479-494 (1999).
15. Sambridge, M. Geophysical inversion with a neighborhood algorithm—II. Appraising the ensemble. *Geophys. J. Int.* **138**, 727-746 (1999).